JAAS

Spatiotemporal Characterization of Cerium Monoxide in Laser Ablation Plasmas using Spectrally-Resolved Fast-Gated Imaging

Journal:	*Journal of Analytical Atomic Spectrometry*
Manuscript ID	JA-ART-12-2023-000441.R1
Article Type:	Paper
Date Submitted by the Author:	14-Feb-2024
Complete List of Authors:	Kwapis, Emily; University of Florida, Hartig, Kyle; University of Florida

Journal Name

ARTICLE TYPE

Cite this: DOI: 00.0000/xxxxxxxxxx

Spatiotemporal Characterization of Cerium Monoxide in Laser Ablation Plasmas using Spectrally-Resolved Fast-Gated Imaging†

Emily H. Kwapis*[a] and Kyle C. Hartig[a]

Received Date
Accepted Date

DOI: 00.0000/xxxxxxxxxx

The impact of oxidation chemistry on the emission characteristics and spatial structure of laser-produced Ce metal plasmas was investigated using laser-induced breakdown spectroscopy (LIBS) and time-resolved fast-gated imaging employing narrowband optical filters. Images of the plasma emission show that CeO coexists with atomic species in the periphery and vortex ring of the plasma plume. Image processing was also applied to combine independent monochromatic images of the plasma emission into a single merged image, culminating in a timelapse on the spatiotemporal evolution of atomic and molecular species within the plasma plume. The formation of CeO species was observed to proceed faster for plasmas generated in atmospheres containing larger concentrations of oxygen based on ratios of CeO-to-atomic emission intensities. These same ratios were shown to plateau and decrease at later times ($\geq$25 μs), potentially indicating the depletion of CeO number densities in the plasma as the monoxide undergoes reactions to form higher polyatomic oxides. Altogether, these results provide fundamental insights into the chemical dynamics and intermixing between plasma-gas species in laser ablation cerium plasmas, advancing our understanding on optical signatures of nuclear-relevant materials to enable in-field measurement capabilities.

1 Introduction

The development of real-time standoff detection methods and optical signatures of nuclear-relevant materials is of great interest to the nuclear nonproliferation and forensics communities, where current research motivations encompass the wide area environmental sampling of actinides to detect undeclared nuclear fuel cycle activities as well as the rapid characterization of post-detonation nuclear environments. Optical spectroscopy techniques using laser-produced micro-plasmas including laser absorption spectroscopy (LAS), laser-induced fluorescence (LIF) spectroscopy, and laser-induced breakdown spectroscopy (LIBS) are viable methods applied towards the standoff characterization of radiological and nuclear materials[1]. Applications range from the spectrochemical assay of gaseous UF_6 for safeguards verification of uranium enrichment levels[2,3] to the monitoring of fission products generated during operations for molten salt reactors[4]. Interactions between aerosols and laser filaments are studied to develop optical signals towards the atmospheric sensing of releases of radiological material[5]. Furthermore, various papers have presented measurements of uranium and plutonium isotope shifts to determine isotopic compositions[2,3,6–8], while others have focused on studying the chemical properties of laser ablation (LA) plasmas to predict fallout formation in nuclear fireballs[9–12].

Chemical reactions in LA plasmas are determined by complex physicochemical interactions between the plasma and surrounding ambient gas. Experimental and quantum chemical investigations (e.g., DFT calculations, second order perturbation theory methods such as CASPT2) on high-temperature gas-phase actinide chemistry suggest that uranium and plutonium react rapidly in oxidizing environments to form simple U_xO_y and Pu_xO_y oxides[13–20], which precede condensation reactions as well as the formation of nanoparticles and larger particulates. The amount of oxygen present in the atmosphere alters the chemical kinetics of the actinide-oxygen system, where the formation of monoxide emission signals has been shown to occur at a faster rate for uranium and plutonium surrogate (cerium) plasmas in atmospheres containing larger mass fractions of oxygen[15,21]. Furthermore, oxygen fugacity impacts chemical reaction pathways and solid-phase end states, leading to the formation of crystalline UO_2 in oxygen deficient atmospheres while the amorphous UO_x (where $3 \leq x \leq 4$) phase is favored at higher oxygen concentrations[11].

Plasma chemical dynamics are strongly influenced by hydrodynamic mechanisms that affect the spatial structures and species distributions of the plasma plume. In the presence of an ambient gas, physical processes such as plume confinement, sharpening,

[a] Nuclear Engineering Program, Department of Materials Science and Engineering, University of Florida, Gainesville, FL 32611, USA. E-mail: ekwapis@ufl.edu

† Electronic Supplementary Information (ESI) available. See DOI: 00.0000/00000000.

splitting, formation of internal plume structures, and the development of fluid instabilities (e.g., Rayleigh-Taylor) affect the properties of the plasma, consequently altering line emission intensities and lifetimes[22–26]. To explain the plasma emission response to this wide range of interconnected factors, the spatial structure and expansion dynamics of the plasma plume (i.e., shape, size, propagation velocity) are frequently studied using time-resolved fast-gated imaging (or fast photography)[27–30]. In addition, imaging of plasma emission using narrowband filters integrated over a limited spectral range provides information on spatial distributions of various species (i.e., atomic, ionic, and molecular) in the plasma plume that can be applied to track molecular formation and chemical interactions between the plasma plume and ambient atmosphere. This approach has been applied to demonstrate that monoxides such as AlO and SrO first form in the cooler periphery of the plasma plume, while other species such as ZrO and UO are more centrally located within the plasma core[31–34]. The spatial distribution of chemical species within laser ablation plasmas is believed to be driven by plasma-gas intermixing processes as well as properties of the molecules themselves, where molecules characterized by higher dissociation energies are able to form in the presence of hotter temperature conditions[32,35,36].

However, while imaging of UO emission and the expansion dynamics of uranium laser-produced plasmas (LPPs) has been performed, equivalent investigations into the oxidation of plutonium LPPs has not yet been conducted despite known differences in chemistry between the two actinide elements. Therefore, this work aims to address this literature gap by explaining the chemical dynamics of plutonium LPPs as a function of varying atmospheric conditions. A common surrogate material for plutonium (i.e., cerium) is used here due to restrictive regulations involving access to and safe handling of plutonium. Laser-induced breakdown spectroscopy is performed to visually demonstrate the significant impact of oxidation reactions on the chemical composition of the plasma plume and its associated spectroscopic signatures, while time-resolved fast-gated imaging is conducted to further investigate the spatial structure of the plasma and spatiotemporal distribution of neutral, ionic, and chemical species within the plume. The results of this work provide insights into the complex gas-phase chemistry and hydrodynamics of plutonium LPPs, supporting the development of nuclear-relevant optical signatures for in-field detection applications in nuclear nonproliferation, safeguards, and forensics.

2 Methodology

2.1 Experimental setup

Cerium ns-LA plasmas are generated using the fundamental wavelength of a Q-switched Nd:YAG laser (Continuum Surelite II-10, 1064 nm, 7 ns pulse duration) with an ablation energy of 60±0.4 mJ. A 100 mm focal-length plano-convex lens is used to focus the laser pulses on the surface of a cerium metal target (MSE Supplies, 99.9% purity) with a crater size of around 500 μm. Laser ablation is performed within a vacuum chamber at atmospheric pressure, where the fill gas is varied between air and argon with various mass fractions of oxygen (Ar for Y_{O_2} = 0, 0.05, 0.10, and 0.20) to control the amount of oxygen available to react with the cerium plasma. To monitor the oxidation chemistry and expansion dynamics of the plasma plume, laser-induced breakdown spectroscopy and time-resolved fast-gated imaging are performed.

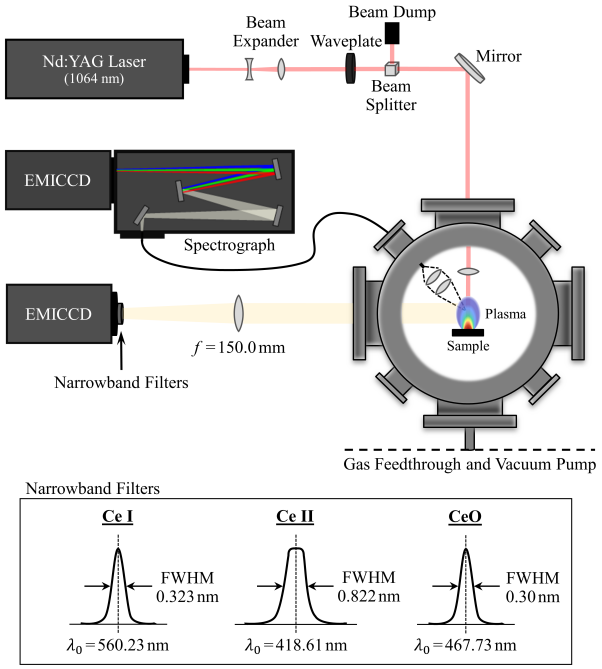

Fig. 1 Experimental setup for laser-induced breakdown spectroscopy and time-resolved fast-gated imaging with ns-LA.

For LIBS, plasma emission light is collected using a pair of uncoated fused silica lenses and directed onto the slit of a Czerny-Turner spectrometer (Princeton Instruments Acton SpectraPro SP-2500) using a 400 μm optical fiber. Broadband measurements are collected between 380 and 670 nm using a 2400 g mm^{-1} grating with a slit width of 50 μm, where instrumental broadening is measured to be 50 pm FWHM at 435.83 nm using a mercury calibration lamp. When collecting spectra for atomic emission (i.e., measurements performed in argon), three shots are averaged to produce each of the individual 44 spectral windows that are stitched together to encompass the entire wavelength range. Measurements targeting molecular emission used ten shots with a higher gain to better resolve CeO bands in the spectrum.

Fast-gated imaging is performed by placing the intensified emICCD camera (Princeton Instruments PI-MAX4: 1024 EMB) orthogonal to the plume expansion direction. A 150 mm focal-length plano-convex lens is used to collect the plasma emission and focus the image onto the camera, providing a magnification of ≈1.2. To obtain spectrally-integrated images of the plasma emission, narrowband optical filters are used independently to target Ce I (560.23 nm/0.323 nm FWHM), Ce II (418.61 nm/0.822 nm FWHM), and CeO emission (467.73 nm/0.30 nm FWHM). Five shots are averaged to produce each image. The experimental setup for both methods is provided in Fig. 1.

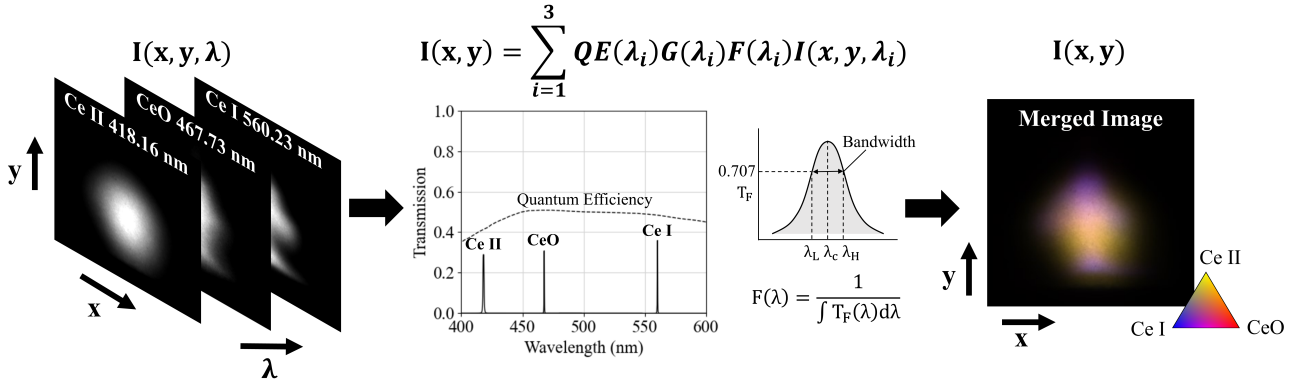

Fig. 2 Process for creating merged images of the plasma emission from individual monochromatic images collected using narrowband optical filters to target Ce I, Ce II, and CeO emission.

2.2 Data analysis and image processing

The fast-gated, spectrally-resolved images of the plasma emission are post-processed by scaling the pixel intensities for each individual image in a set (i.e., atmospheric parameter such as 760 Torr Ar with $Y_{O_2} = 0.05$) to the same scale to enable a direct comparison between images collected at the same time delay using different monochrome filters. During this process, the measured pixel intensities are adjusted according to Eq. 1,

$$I(x,y) = \sum_{i=1}^{3} G(\lambda_i)GW(\lambda_i)F(\lambda_i)QE(\lambda_i)I(x,y,\lambda_i) \quad (1)$$

where $G(\lambda_i)$, $GW(\lambda_i)$, $F(\lambda_i)$, and $QE(\lambda_i)$ represent the scaling factors to correct for differences in gain, gate width, filter transmissivity and bandwidth, and quantum efficiency of the emICCD for each of the three filters used during imaging. The scaling factor for the gain, $G(\lambda_i)$, is based an empirical equation obtained by measuring the spectral response of the camera using a tungsten light source. A scaling factor, $F(\lambda_i)$, is defined for the optical filters because filters with larger bandwidths and higher transmissions pass a greater quantity of light to the camera. The measured pixel intensities are corrected for differences in filter properties by dividing by the integrated filter transmission, which is determined from the measured bandwidth and peak transmission provided by the manufacturer. Subsequent to correcting the pixel intensities, false color is assigned to each filter (Ce I → blue, Ce II → yellow, CeO → red) and the spectrally-resolved images at each time delay are overlaid and combined into a single image. This process is repeated for each time delay measured, resulting in a visual representation of the dynamic populations of neutral, ionic, and molecular species in the plasma over time. A flowchart further explaining this image processing approach is shown in Fig. 2. Beyond the analysis of LA plasmas, this image processing technique of combining individual monochromatic images into a single merged image is frequently applied towards applications in astronomy, remote sensing, and microscopy[37–41].

3 Results and discussion

The measurement of optical signatures in the field requires an informed understanding of the impact of oxidation chemistry on recorded signatures of LA plasmas. In relation to laser-produced cerium plasmas, high-temperature gas-phase oxidation pathways involve the reaction of atomic Ce with oxygen to initially form CeO followed by the formation of polyatomic cerium oxides and nanoparticles as the plasma cools. The early-time chemistry and formation of CeO is investigated in this work using emission spectroscopy, where CeO signals are recorded and observed to persist until around 75 μs. The affect of CeO formation on spectroscopic signatures is first demonstrated by performing broadband LIBS measurements under inert and oxidizing conditions (i.e., argon versus air), where a comparison of these measurements emphasizing significant changes to the spectrum in the presence of oxygen is shown in Fig. 3. The spectrum recorded in argon consists of narrow Voigt-shaped peaks corresponding to Ce I and Ce II emission lines, while the measurement collected in air is dominated by broader triangular lineshapes associated with molecular signatures of cerium oxide. These molecular signatures overlap with atomic emission lines, complicating the deconvolution of the spectrum and obscuring most atomic lines by a time delay of 20 μs.

CeO signals have previously been recorded over limited spectral regions (e.g., 466-472, 484-490, and 723-735 nm) using LIBS to study the oxidation chemistry of Ce LA plasmas[12,21]. Among the band assignments provided in these publications include the B_2-X_2, D_1-X_1, and D_3-X_3 CeO transitions[12,21]. A wider spectral region between 380-670 nm is covered in this work in an effort to identify additional strong CeO bands in the LIBS spectrum that may potentially be useful towards studying the chemical dynamics of Ce LA plasmas. Transition labels are assigned to recorded molecular features for the Ce LIBS spectrum collected in air based on previous reports provided in the literature[42–46]. Rudimentary theoretical simulations of the molecular spectra are also performed using PGopher for the transitions where molecular constants were available. However, it should be understood that these simulations are very limited and only provide general insights into the energies and shapes of the CeO bands, where more advanced and accurate models were unable to be produced due to errors associated with the reported constants as well as the lack of data on additional parameters such as coupling constants and line-strength factors.

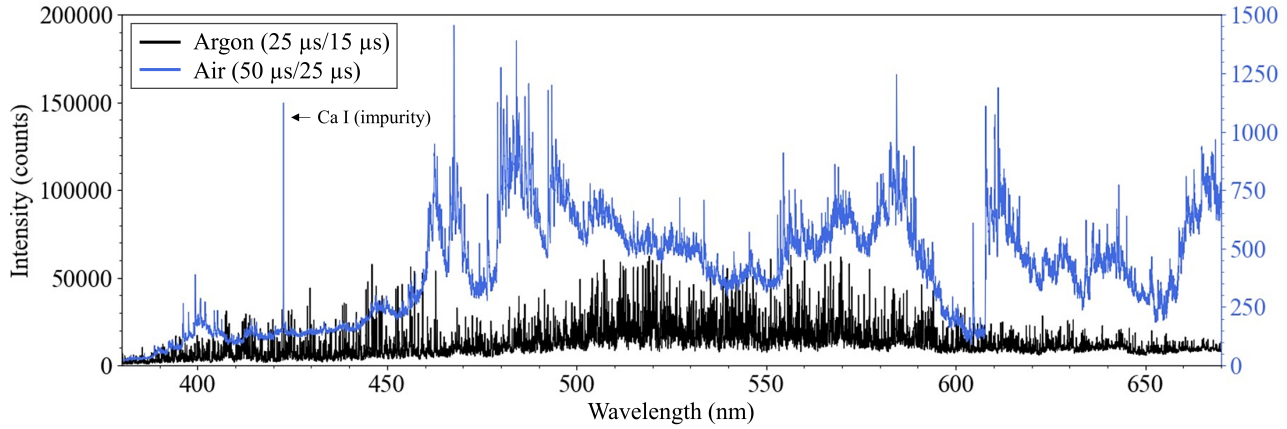

Fig. 3 Comparison between broadband spectroscopic signatures for atomic cerium and cerium oxide recorded at atmospheric pressure in argon and air atmospheres, respectively. Time delays and gate widths for the measurements are indicated in the figure caption as delay/width.

Ro-vibronic transition assignments are provided in Fig. 4, where the head-forming branches are indicated when they are known. CeO bands identified in the spectrum include the B_1-X_1, C_3-X_3, D_1-X_1, D_3-X_3, E_1-X_1, E_2-X_2, E_3-X_3, F_2-X_2, g_2-X_2, and G_2-X_2 transitions. Generally, the R and Q branches of these bands are recognizable as distinctive sawtooth patterns in the spectrum, while the P branches are present as broader signals characterized by lower intensities that present themselves by contributing baseline to the spectrum. Unlabeled molecular transitions between 480 – 486 nm are believed to correspond to several CeO bands originating from different energies levels ([22.5]1-$V_1 0^-$, m_4-m)†. Hot bands associated with the F_2-X_2 transition are also present over this spectral window, further complicating the deconvolution of the molecular spectrum. Typically, several hot bands for each ro-vibronic transition are observed, which is expected because the plasma temperature is realistically at least a few thousand Kelvin based on LA plasma properties typically reported in the literature for comparable experimental conditions[32,47,48]. PGopher is used to assist in the identification of several of these band sequences involving excited states, such as the D_3-X_3 $\Delta v=+1$ fundamental band and hot bands. The 1-1 and 2-2 band sequences of the E_1-X_1 transition and 2-2 band of the E_3-X_3 transition are also identified through this method. Overtones may also be present in the spectrum, although none are formally assigned here.

CeO bands of the greatest interest for studying oxidation chemistry in LA plasmas are those with at least one head-forming branch that does not overlap with strong neutral or ionic emission lines. Candidates that satisfy this requirement are the R branch of the B_1-X_1 0-0 transition, the Q branch of the D_1-X_1 0-0 transition, the R branch of the G_2-X_2 0-0 transition, where only electronic transitions between the lowest vibrational levels (i.e., 0-0) are considered here because they are characterized by larger intensities than the other molecular transitions present in the spectrum. The G_2-X_2 transition is consistently measured to be weaker in intensity than the B_1-X_1 and D_1-X_1 transitions that are tied to the ground state, while the D_1-X_1 band is the strongest molecular transition recorded in the spectrum. Therefore, the Q branch of the D_1-X_1 transition was targeted to image CeO emission in the LA plasma plume using a custom narrowband filter centered on the branch head.

3.1 Plasma plume structure

Laser ablation plasmas can be described as high-temperature gas-dynamic flows that initially expand outwards very rapidly. In the presence of an ambient gas, this rapid expansion is analogous to a fast-moving mass of dense fluid traveling into a less dense and stationary fluid. During this process, a viscous friction force is experienced at the interface between these two fluids (i.e., the plume front) that works to slow down the outer layers of the fast-moving fluid relative to its core[49]. These outer layers then slide behind the faster-moving inner layers to the base of the flow where they are pulled back up into (or rolled into) the core of the plume, ultimately leading to the formation of a torus and mushroom-like head that is more formally known as a vortex ring[49,50]. In this work, plasma plumes are first observed to be marked by a mushroom-like morphology around 500 ns, while the torus continues to develop over a timescale of several microseconds (see Fig. 5). Various publications in the literature have also reported images on vortex formation in laser ablation plasmas over various timescales (<500 ns or as late as >50 μs) depending on ablation conditions and target material properties[30,51–54]. Fundamental studies on fluid dynamics and vortex formation also suggest that when a fluid is impulsively ejected through a narrow aperture that the fluid will interact with the edges of the opening by curling in on itself, ultimately leading to the formation of a vortex ring[49,55]. Therefore, it is valuable to consider the crater generated during laser ablation as an analog to this aperture and second factor impacting vortex formation in LA plasmas. While the imaging setup used in this work is unable to resolve details on the spatial structure of the plasma plume at very early times post-LA, simulations provided by Kwapis *et al.* in a previous publication support the existence of this phenomenon in the expansion dynamics of LA

† The notation used for the excited state [22.5]1 follows that used by both Linton *et al.* and Kaledin *et al.*, and represents a term energy around 22,500 cm^{-1} and $\Omega=1$[45,46].

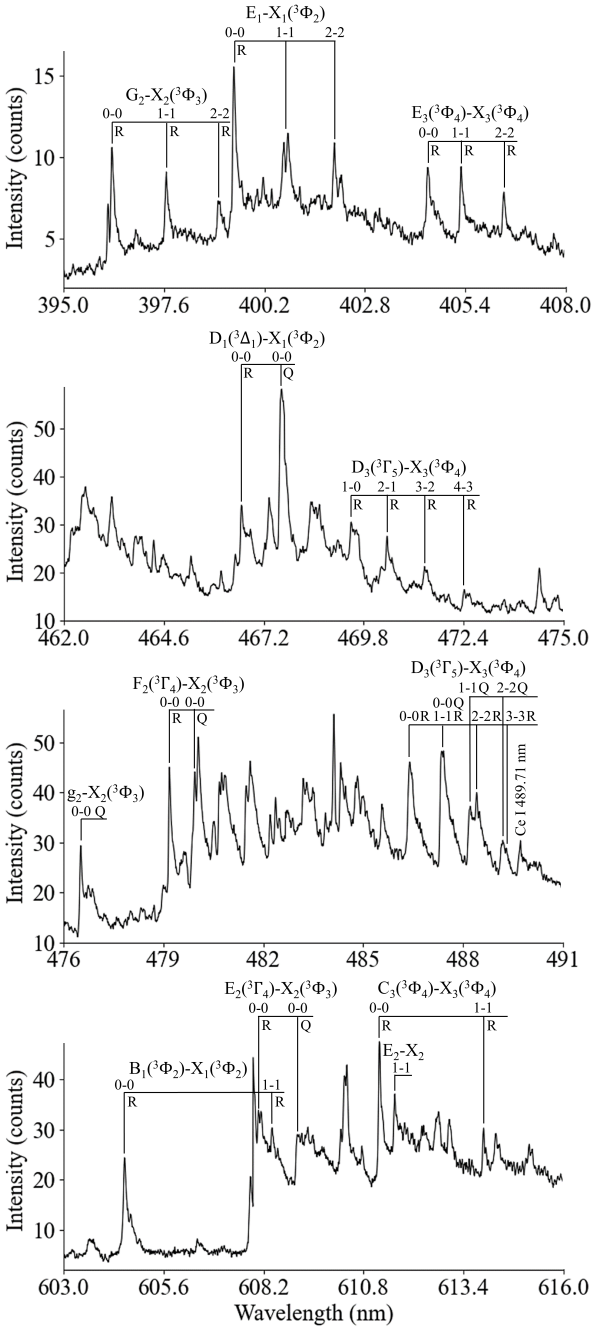

Fig. 4 CeO bands identified in the visible spectrum using LIBS. The head-forming branch is indicated when it is known.

plasmas[32].

The spatial distribution of atomic and molecular species in the plasma plume is also shown in Fig. 5, where based on the spectrally-resolved images of the plasma emission ionic species are observed to be confined predominately within the head of the plasma plume, while Ce I is more prevalent within the stem, vortices, and top of the plume head. Images of CeO emission show that the formation of molecular species is favored at the top of the plume head for the first 2.5 μs before advancing to the vortices of the plume around 5 – 15 μs. Vortex formation is believed to result in enhanced intermixing between the plasma and its surrounding atmosphere, augmenting chemical reactions within the plasma plume[56,57]. Cerium monoxide is also believed to coexist in the periphery of the plume with atomic Ce as well based on the images provided in Fig. 5. Monoxide formation is frequently reported to occur at the interface between the plume and background gas for laser ablation plasmas, where this chemical process is driven by concentration gradients, diffusion processes, and lower plasma temperatures in the plume periphery[31,32,58,59]. Molecular formation in the vortices of the plasma plume resulting from fluid hydrodynamics is less commonly reported on in the literature due to difficulties in resolving the torus in fast-gated, spectrally-resolved images of the plasma emission. Instead, molecular species may be described as forming volumetrically within the plasma or closer to the core of the plasma plume[33,34]. Multiphysics modeling using a reactive computational fluid dynamics (CFD) code has demonstrated the formation of several gas-phase oxide phases within the vortices of aluminum vapor plumes in air[32].

As the plasma plume continues to evolve over time, heat is transferred from the plasma to the surrounding atmosphere through conduction and the entrainment of ambient gas into the plume until the plume ultimately collapses and diffuses into the surrounding atmosphere[60]. In this work, this process is visually observed to begin around 20 μs when the plume size starts decreasing and the vortex ring recombines into a single non-toroidal structure. Over this timescale, Ce I and CeO species are observed to occupy the same spatial region within the plume while Ce II species tend to be located within the upper half of the plume. Polyatomic oxide formation and condensation reactions will also proceed at later times, where these species will coexist in the plasma plume with atomic Ce and CeO.

3.2 Chemical dynamics

To further characterize the spatiotemporal evolution of CeO formation in laser-induced cerium plasmas, spectrally-resolved imaging of the plasma emission was performed in argon atmospheres containing different concentrations of oxygen ranging from oxygen mass fractions of $Y_{O_2} = 0 - 0.20$. The results of these measurements are presented in Fig. 6 alongside measurements collected in air. Ce II emission is observed to dominate for the earliest time delays shown in figure (i.e, 1 and 2 μs) for all fill gases used in this work, indicating that the ion number density is greater than that for neutral and molecular species assuming that emission signals are proportional to species number densities in the plasma. Ce I emission is observed to emerge earlier during the evolution process for plasmas generated in air as compared to argon, which may be an indication of lower plasma temperatures. Further discussion on this will be included at the end of this section.

For the argon atmospheres, Ce I emission becomes more comparable in intensity to Ce II emission between 5 – 10 μs based on the image color shifting to a mix between blue (i.e., Ce I) and yellow (i.e., Ce II). This progression is delayed for the pure argon atmosphere, where ionic emission remains predominate un-

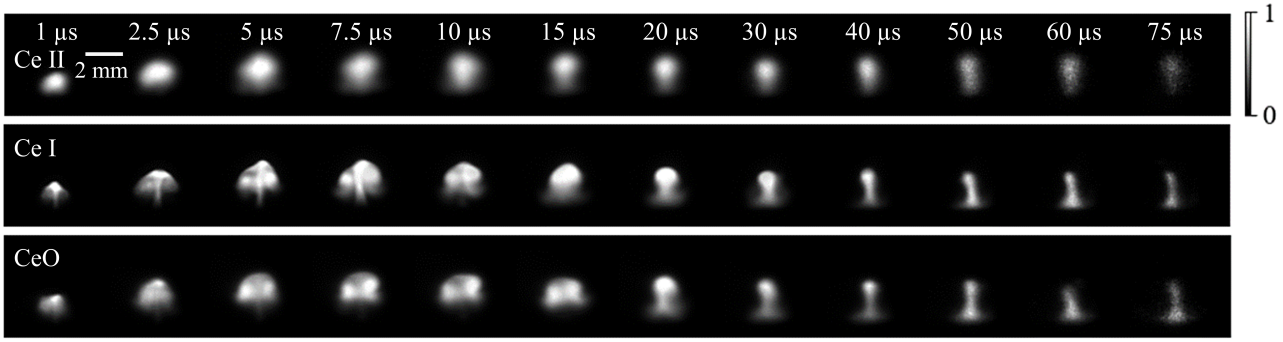

Fig. 5 Time-resolved fast-gated images of Ce LPP plasma emission in argon with Y_{O_2} = 0.20 at atmospheric pressure. Each individual frame is normalized to its minimum and maximum pixel intensities.

til around 15 μs after laser ablation. Longer-lived ionic emission in the pure argon atmosphere is attributed to the very limited oxidation of the Ce plasma compared to the argon-oxygen gas mixtures, where oxidation reactions are still specified as present due to oxygen contained within the oxide layer on the metal sample. For the argon atmospheres containing oxygen (i.e., Ar with Y_{O_2} = 0.05, 0.10, and 0.20), CeO emission is visible and comparable in strength to atomic Ce emission starting around 25 μs based on the purple-colored plumes observed in Fig. 6. These results are in agreement with a previous publication covering LIBS measurements of Ce metal, where CeO signals were observed to be more prominent than atomic emission lines in the spectrum starting around 20–25 μs[21].

Differences in the plasma shapes at later times (>25 μs) between measurements for Y_{O_2} = 0.05 and Y_{O_2} = 0.10 are not a result of oxidation reactions in the Ce plasma. Ablation conditions were unfortunately altered between these measurements due to the concave lens in the beam expander shown in Fig. 1 becoming burned during the middle of the experiment, thereby requiring the lens to be replaced. The spot size at the sample surface is believed to be altered as a result of this replacement, consequently changing the morphology of the plasma plume. The position of the sample was adjusted to mitigate these changes to the plume morphology in order to maintain comparable plasma properties between all measurements, although small differences remain.

A more quantitative analysis may also be performed in addition to visually comparing the merged images of the Ce plasma emission. This is done by averaging the pixel intensities over the plasma plume in each of the monochromatic images followed by a comparison of the mean pixel intensities. The plasma plume is defined based on a thresholding procedure, where all pixels with intensities greater than 10% of the maximum pixel intensity in the image are assigned to the plasma and all remaining pixels correspond to background. Fig. 7 shows ratios of mean intensities for CeO emission compared to Ce I and Ce II emission. CeO-to-Ce II ratios are intrinsically larger than those reported for Ce I because Ce II emission is consistently weaker than Ce I emission past 5 μs after laser ablation. Ratios are also tied to the specific transitions selected to produce the curves and will vary between individual transitions from the same ionization state (e.g., Ce II 418.66 nm versus Ce II 428.99 nm) simply based on the different decay behaviors for the transitions involved. Overall, the ratio curves represent CeO formation within the plasma, where the general trends and shapes of the curves are more informative than the actual ratio values.

All molecular-to-atomic emission intensity ratio curves are observed to increase initially, representing the early growth of CeO in the plasma as number densities for Ce I and Ce II decrease due to recombination and chemical reactions. This behavior resembles analogous ratio curves obtained from LIBS measurements of Ce LPPs reported in Ref. 21, where this publication was only able to cover around the first 30 μs after laser ablation before peaks for the selected atomic transitions could no longer be resolved in the recorded spectra. In this same publication, CeO formation is observed to proceed faster for oxygen mass fractions between Y_{O_2} = 0.10 – 0.15 in argon, which is indicated by larger ratios[21]. In this work, chemistry is generally observed to proceed faster for Y_{O_2} = 0.10 – 0.20 for earlier times (<25 μs) until these curves begin to plateau and ratios for Y_{O_2} = 0.05 are reported as consistently larger than the other curves. CeO growth trends between these two separate experiments agree decently with each other, while minor dissimilarities can be attributed to inherent fluctuations in LA plasma properties measured on different days and differences in ambient pressure (100 Torr for the LIBS measurements versus 760 Torr for the time-resolved imaging measurements). Consistently larger molecular-to-atomic emission intensity ratios for Y_{O_2} = 0.05 at later times ($\geq$ 25 μs) may indicate that CeO formation proceeds at a slower rate when oxygen is limited, where this behavior has been reported for both uranium and cerium LA plasmas[15,21]. The plateauing behavior as well as decreasing intensity ratios at later times may be an indicator that the number density of CeO within the plasma is decreasing, which can be attributed to CeO serving as a reactant for the formation of polyatomic oxides (Ce_xO_y).

Curves for CeO formation in air are also provided alongside those for the argon-oxygen atmospheres in Fig. 7, where molecular-to-atomic emission intensity ratios are consistently larger in air for earlier times (<20 μs) during the evolution of the plasma. Lower plasma temperatures and electrons densities are expected for LA plasmas generated in air as compared to argon because the lower gas density characterizing air ($\rho_{air} < \rho_{Ar}$) will provide reduced confinement on the plasma plume[61]. Con-

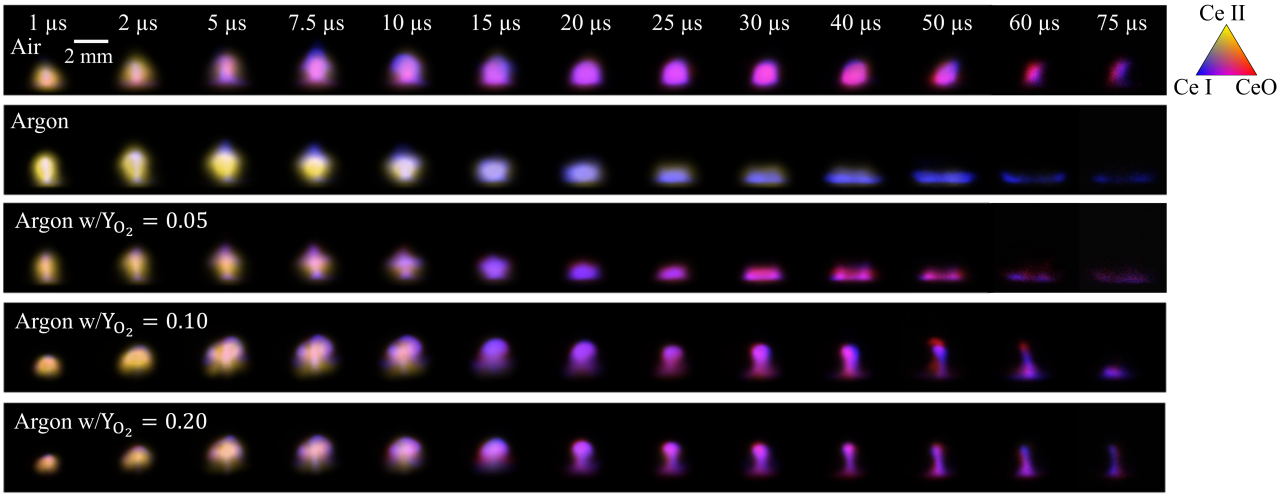

Fig. 6 Merged images of Ce LPP plasma emission that demonstrate the spatiotemporal evolution of atomic and molecular species within the plasma plume for different atmospheric conditions. Differences in plume morphology between argon atmospheres with $Y_{O_2} = 0.05$ and $Y_{O_2} = 0.10$ are a result of a minor alteration to the experimental setup and are not related to plasma chemistry effects.

versely, hotter plasma temperatures will hinder chemical reactions within the plasma until later times when temperature conditions are cooler, thereby explaining the limited CeO formation in the argon-oxygen gas mixtures at earlier times when compared to air.

4 Conclusions

The spatiotemporal characterization of CeO in cerium LPPs was performed to investigate the underlying chemical dynamics that drive changes to the plasma composition and associated spectroscopic signatures over time. Resolved images on the internal structure of the plasma plume revealed that CeO formation occurs in both the periphery and vortex ring of the plume, indicating that the oxidation chemistry of cerium plasmas is driven by both diffusion and hydrodynamic processes. These observations provide important advancements towards understanding the underlying mixing dynamics between plasma and ambient gas species that control molecular formation in LA plasmas.

To further control the interaction of the plasma with oxygen in its surrounding environment, oxygen mass fractions in argon gas were varied between 0 – 0.20. Monochromatic images of the plasma emission for Ce I, Ce II, and CeO were then combined into a single merged image at each time delay to provide a color-coded representation on the spatiotemporal evolution of atomic and molecular species in the plasma plume over time. Ionic emission was shown to dominate the plasma plume at early times while CeO emission becomes predominate at later times. Ratios of CeO-to-atomic emission intensities extracted from the images also showed faster CeO formation for atmospheres containing larger concentrations of oxygen, agreeing with previously published spectroscopic measurements of laser-produced cerium plasmas subject to similar experimental parameters and environmental conditions. Furthermore, the ratios reported in this work were observed to plateau and decrease at later times ($\geq$25 μs), possibly indicating the formation of polyatomic cerium oxides (Ce_xO_y) in the plasma plume. Collectively, these measurements

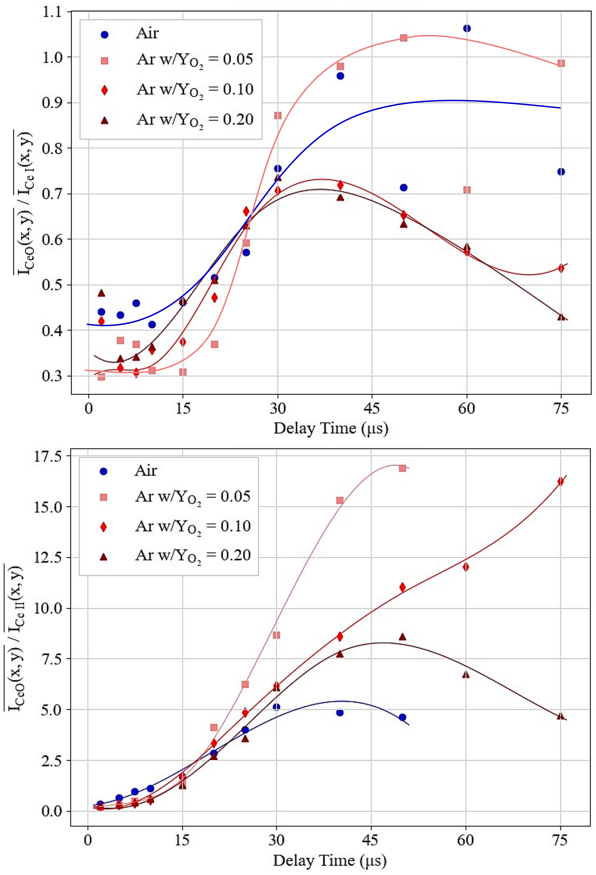

Fig. 7 CeO formation curves based on ratios between mean pixel intensities extracted from spectrally-integrated images for (top) CeO 467.73 nm and Ce I 560.13 nm and (bottom) CeO 467.73 nm and Ce II 418.66 nm. Spline curves overlaid on the data points are drawn for visualization purposes only. Errorbars are unable to be provided with the data because the software used to collect the images omitted statistics after exporting an average of several laser shots. Shot-to-shot variations for the recorded images range from a few thousand counts for plasmas generated at the same crater up to 10,000 counts between different craters for raw pixel intensities. Associated errors are realistically as large as 30%.

and observations on the high-temperature combustion chemistry and hydrodynamics of plutonium surrogate (cerium) LA plasmas provide relevant insights into gas-phase debris formation chemistry subsequent to the detonation of a nuclear device as well as the impact of oxidizing atmospheres on the plasma composition and its associated optical signatures.

Author Contributions

Emily H. Kwapis Investigation (lead); Formal analysis (lead); Methodology (equal); Software (lead); Validation (equal); Visualization (lead); Writing – original draft (lead); Writing – review and editing (equal). **Kyle C. Hartig** Conceptualization (lead); Methodology (equal); Validation (equal); Writing – review and editing (equal); Funding acquisition (lead); Project administration (lead); Resources (equal); Supervision (lead).

Conflicts of interest

There are no conflicts of interest to declare.

Acknowledgements

This document is the result of research funded partially by the Department of Defense Science, Mathematics, and Research for Transformation (SMART) Scholarship-for-Service Program; US Department of Energy (DOE) National Nuclear Security Administration Monitoring, Technology, and Verification (MTV) Consortium award number DE-NA0003920 and Consortium for Nuclear Forensics award number DE-NA0004142; and Defense Threat Reduction Agency award numbers HDTRA1-20-2-0002. The content of the information does not necessarily reflect the position or the policy of the federal government, and no official endorsement should be inferred.

Notes and references

1 E. Kwapis, J. Borrero, K. Latty, H. Andrews, S. Phongikaroon and K. Hartig, Laser Ablation Plasmas and Spectroscopy for Nuclear Applications, *App. Spec.*, 2024, **78**, In–Press.

2 G. Chan, K. Peruski and L. Martin, Laser-Induced Spectrochemical Assay for Uranium Enrichment (LISA-UE), Proc. of the INMM & ESARDA Joint Virtual Annual Meeting, 2021.

3 G. C.-Y. Chan, X. Mao, L. R. Martin, L. D. Trowbridge and R. E. Russo, Direct Uranium Enrichment Assay in Gaseous Uranium Hexafluoride with Laser Induced Breakdown Spectroscopy, *J. Radioanal. Nucl. Chem.*, 2022, **331**, 1409–1421.

4 H. Andrews, J. McFarlane and K. Myhre, Monitoring Nobel Gases (Xe and Kr) and Aerosols (Cs and Rb) in a Molten Salt Reactor Surrogate Off-Gas Stream using Laser-Induced Breakdown Spectroscopy (LIBS), *Appl. Spectrosc.*, 2022, **76**, 988–997.

5 K. Latty and K. Hartig, Spatiotemporal Plasma-Particle Characterization of Dry Aerosols using Nanosecond, Femtosecond, and Filament Laser-Produced Plasmas, *Appl. Spectrosc.*, 2022, **0**, 1–12.

6 S. F. Boulyga, J. S. Becker, J. L. Matusevitch and H.-J. Dietze, Isotope Ratio Measurements of Spent Reactor Uranium in Environment Samples by Using Inductively Coupled Plasma Mass Spectrometry, *Int. J. Mass Spectrom.*, 200, **203**, 143–154.

7 J. Song, G. C.-Y. Chan, X. Mao, J. D. Woodward, R. W. S. III, T. G. Schaaff, A. C. Stowe, C. D. Harris, R. Zheng, V. Zorba and R. E. Russo, Multivariate Nonlinear Spectral Fitting for Uranium Isotopic Analysis with Laser-Induced Breakdown Spectroscopy, *Spectrochim. Acta Part B: At. Spectrosc.*, 2018, **150**, 67–76.

8 C. A. Smith, M. A. Martinez, D. K. Veirs and D. A. Cremers, Pu-239/Pu-240 Isotope Ratios Determined using High Resolution Emission Spectroscopy in a Laser-Induced Plasma, *Spectrochim. Acta Part B: At. Spectrosc.*, 2002, **57**, 929–937.

9 B. Koroglu, S. Wagnon, Z. Dai, J. C. Crowhurst, M. R. Armstrong, D. Weisz, M. Mehl, J. M. Zaug, H. B. Radousky and T. P. Rose, Gas-Phase Chemical Evolution of Uranium, Aluminum, and Iron Oxides, *Sci. Rep.*, 2018, **8**, 10451.

10 B. Koroglu, Z. Dai, M. Finko, M. Armstrong, J. Crowhurst, D. Curreli, D. Weisz, H. Radousky, K. Knight and T. Rose, Experimental Investigation of Uranium Volatility during Vapor Condensation, *Anal. Chem.*, 2020, **92**, 6437–6445.

11 M. Burton, A. Auner, J. Crowhurst, P. Boone, L. Finney, D. Weisz, B. Koroglu, I. Jovanovic, H. Radousky and K. Knight, The Effect of Oxygen Concentration on the Speciation of Laser Ablated Uranium, *Sci. Rep.*, 2022, **12**, 4030.

12 K. Rodriguez, B. Koroglu, J. Hammons, Z. Dai, M. G. Ferrier, E. Balboni, T. Rose and K. B. Knight, Vapor-Phase Aggregation of Cerium Oxide Nanoparticles in a Rapidly Cooling Plasma, *ACS Earth Space Chem.*, 2022, **6**, 1997–2008.

13 K. Hartig, S. Harilal, M. Phillips, B. Brumfield and I. Jovanovic, Evolution of Uranium Monoxide in Femtosecond Laser-induced Uranium Plasmas, *Opt. Express*, 2017, **25**, 11477.

14 K. C. Hartig, I. Ghebregziabher and I. Jovanovic, Standoff Detection of Uranium and its Isotopes by Femtosecond Filament Laser Ablation Molecular Isotopic Spectrometry, *Sci. Rep.*, 2017, **7**, 43852.

15 S. Harilal, E. Kautz, B. Bernacki, M. Phillips, P. Skrodzki, M. Burger and I. Jovanovic, Physical Conditions for UO Formation in Laser-produced Uranium Plumes, *Phys. Chem. Chem. Phys.*, 2019, **21**, 16161.

16 P. Skrodzki, M. Burger, I. Jovanovic, M. Phillips, B. Brumfield and S. Harilal, Tracking of Oxide Formation in Laser-Produced Uranium Plasmas, *Opt. Lett.*, 2018, **43**,.

17 H. Yousfi, N. el Houda Bensiradj, M. Khedidji, A. Saal and O. Ouamerali, Theoretical Investigation of the Structure and Spectroscopy of Uranium Oxide Species, *Theor. Chem. Acc.*, 2023, **142**, 5.

18 A. Kovács, R. J. Konings, J. K. Gibson, I. Infante and L. Gagliardi, Quantum Chemical Calculations and Experimental Investigations of Molecular Actinide Oxides, *Chem. Rev.*, 2015, **115**, 1725–1759.

19 G. L. Macchia, I. Infante, J. Raab, J. K. Gibson and L. Gagliardi, A Theoretical Study of the Ground State and Lowest Excited States of $PuO^{0/+/+2}$ and $PuO_2^{0/+/+2}$, *Phys. Chem. Chem. Phys.*, 2008, **10**, 7278–7283.

20 A. V. Zaitsevskii, A. V. Titov, S. S. Mal'kov, I. G. Tananaev and Y. M. Kiselev, On the Existence of Oxide Molecules of Plutonium in Highest Oxidation States, *Dokl. Chem.*, 2013, **448**,.

21 E. H. Kwapis, E. Villa-Aleman and K. C. Hartig, Spectroscopic Signatures and Oxidation Characteristics of Nanosecond Laser-Induced Cerium Plasmas, *Spectrochim. Acta. Part. B At. Spectrosc.*, 2023, **200**, 106610.

22 P. K. Diwakar, S. S. Harilal, M. C. Phillips and A. Hassanein, Characterization of Ultrafast Laser-Ablation Plasma Plumes at Various Ar Ambient Pressures, *J. Appl. Phys.*, 2015, **118**, 043305.

23 S. Harilal, C. Bindhu, M. Tillack, F. Najmabadi and A. Gaeris, Plume Splitting and Sharpening in Laser-Produced Aluminum Plasma, *J. Phys. D: Appl. Phys.*, 2002, **35**, 2935–2938.

24 S. Harilal, C. Bindhu, M. Tillack, F. Najmabadi and A. Gaeris, Internal Structure and Expansion Dynamics of Laser Ablation Plumes into Ambient Gases, *J. Appl. Phys.*, 2003, **93**, 2380–2388.

25 S. Abdelli-Messaci, T. Kerdja, S. Lafane and S. Malek, Fast Imaging of Laser-Induced Plasma Emission from a ZnO Target, *Spectrochim. Acta Part B: At. Spectrosc.*, 2009, **64**, 968–973.

26 N. LaHaye, S. Harilal, P. Diwakar and A. Hassanein, Persistence of Uranium Emission in Laser-Produced Plasmas, *J. Appl. Phys.*, 2014, **115**, 163301.

27 D. B. Geohegan and A. A. Puretzky, Laser Ablation Plume Thermalization Dynamics in Background Gases: Combined Imaging, Optical Absorption and Emission Spectroscopy, and Ion Probe Measurements, *Appl. Surf. Sci.*, 1996, **96-98**, 131–138.

28 J. Freeman, S. Harilal, P. Diwakar, B. Verhoff and A. Hassanein, Comparison of Optical Emission from Nanosecond and Femtosecond Laser Produced Plasma in Atmosphere and Vacuum Conditions, *Spectrochim. Acta Part B: At. Spectrosc.*, 2013, **87**, 43–50.

29 E. J. Kautz, D. J. Senor and S. S. Harilal, The Interplay between Laser Focusing Conditions, Expansion Dynamics, Ablation Mechanisms, and Emission Intensity in Ultrafast Laser-Produced Plasmas, *J. Appl. Phys.*, 2021, **130**, 204901.

30 A. Auner, J. Crowhurst, L. Nagel, D. Weisz, A. Rousso and K. Knight, Fast Imaging of Laser Ablation of Cerium: Dependence of Plasma Plume Dynamics and Structure on Native Oxide Growth, *AIP Adv.*, 2022, **12**, 065119.

31 E. R. Wainwright, S. W. Dean, F. C. D. L. Jr., T. P. Weihs and J. L. Gottfried, Effect of Sample Morphology on the Spectral and Spatiotemporal Characteristics of Laser-Induced Plasmas from Aluminum, *Appl. Phys. A*, 2020, **126**, 83.

32 E. H. Kwapis, J. W. Posey, E. Medici, K. Berg, R. W. Houim and K. C. Hartig, Experimental and Computation Investigation into the Hydrodynamics and Chemical Dynamics of Laser Ablation Aluminum Plasmas, *Phys. Chem. Chem. Phys.*, 2023, **25**, 15666–15675.

33 D. Weisz, J. Crowhurst, M. Finko, T. Rose, B. Koroglu, R. Trappitsch, H. Radousky, W. Siekhaus, M. Armstrong, B. Isselhardt, M. Azer and D. Curreli, Effects of Plume Hydrodynamics and Oxidation on the Composition of a Condensing Laser-Induced Plasma, *J. Phys. Chem. A*, 2018, **122**, 1584–1591.

34 E. Kautz, P. Skrodzki, M. Burger, B. Bernacki, I. Jovanovic, M. Phillips and S. Harilal, Time-Resolved Imaging of Atoms and Molecules in Laser-Produced Uranium Plasmas, *J. Anal. At. Spectrom.*, 2019, **34**, 2236.

35 E. R. Wainwright, F. C. De Lucia, T. P. Weihs and J. L. Gottfried, Spatiotemporal and Emission Characteristics of Laser-Induced Plasmas from Aluminum-Zirconium Composite Powders, *Spectrochim. Acta Part B: At. Spectrosc.*, 2021, **183**, 106270.

36 A. D. Giacomo and J. Hermann, Laser-Induced Plasma Emission: From Atomic to Molecular Spectra, *J. Phys. D: Appl. Phys.*, 2017, **50**, 183002.

37 T. A. Rector, Z. G. Levay, L. M. Frattare, K. K. Arcand and M. Watzke, The Aesthetics of Astrophysics: How to Make Appealing Color-Composite Images that Convey the Science, *PASP*, 2017, **129**, 058007.

38 D. G. Manolakis, R. B. Lockwood and T. C. Cooley, *Hyperspectral Imaging Remote Sensing: Physics, Sensors, and Algorithms*, Cambridge University Press, 1st edn, 2016.

39 L. Gao and R. T. Smith, Optical Hyperspectral Imaging in Microscopy and Spectroscopy – A Review of Data Acquisition, *J Biophotonics*, 2015, **8**, 441–456.

40 P. Favreau, C. Hernandez, A. S. Lindsey, D. F. Alvarez, T. Rich, P. Prabhat and S. J. Leavesley, Thin-Film Tunable Filters for Hyperspectral Fluorescence Microscopy, *J. Biomed. Opt.*, 2014, **19**, 011017.

41 K. Hamada, K. Fujita, N. I. Smith, M. Kobayashi, Y. Inouye and S. Kawata, Raman Microscopy for Dynamic Molecular Imaging of Living Cells, *J. Biomed. Opt.*, 2008, **13**, 044027.

42 R. Barrow, R. Clements, S. Harris and P. Jenson, The Electronic Spectrum of Gaseous CeO, *ApJ*, 1979, **229**, 439–447.

43 S. Wyckoff and P. Wehinger, CeO: A New s-Process Molecule in S Stars?, *ApJ*, 1977, **212**, L139–L141.

44 C. Linton, M. Dulick, R. Field, P. Carette and R. Barrow, Low Lying Electronic States of CeO, *J. Chem. Phys.*, 1981, **74**, 189–191.

45 L. Kaledin, J. McCord and M. Heaven, Laser Spectroscopy of CeO: Characterization and Assignment of States in the 0-3 eV Range, *J. Mol. Spectrosc.*, 1993, **158**, 40–61.

46 C. Linton, M. Dulick, R. Field, P. Carette, P. Leyland and R. Barrow, Electronic States of the CeO Molecule: Absorption, Emission, and Laser Spectroscopy, *J. Mol. Spectrosc.*, 1983, **102**, 441–497.

47 C. G. Parigger, A. C. Woods, A. Keszler, L. Nemes and J. O. Hornkohl, Titanium Monoxide Spectroscopy Following Laser-Induced Optical Breakdown, *AIP Conf. Proc.*, 2012, **1464**, 628–639.

48 X. Bai, V. Motto-Ros, W. Lei, L. Zheng and J. Yu, Experimental Determination of the Temperature Range of AlO Molecular Emission in Laser-Induced Aluminum Plasma in Air, *Spectrochim. Acta Part B: At. Spectrosc.*, 2014, **99**, 193–200.

49 W. Rogers, On the Formation of Rotating Rings by Air and Liq-

uids under Certain Conditions of Discharge, *Am. J. Sci. Arts*, 1858, **26**, 246–258.

50 A. Glezer, The Formation of Vortex Rings, *Phys. Fluids*, 1988, **31**, 3532–3542.

51 M. Finko, J. C. Crowhurst, W. J. Keller, A. C. Rousso, S. S. Ly, D. G. Weisz, D. Curreli, H. B. Radousky and K. B. Knight, Investigating Laser Ablated Plume Dynamics of Carbon and Aluminum Targets, *Phys. Plasmas*, 2022, **29**, 083506.

52 T. Schmitz, J. Koch, D. Günther and R. Zenobi, Characterization of Aerosol Plumes in Nanosecond Laser Ablation of Molecular Solids at Atmospheric Pressure, *Appl. Phys. B*, 2010, **100**, 521–533.

53 S. Heiroth, J. Koch, T. Lippert, A. Wokaun, D. Günther, F. Garrelie and M. Guillermin, Laser Ablation Characteristics of Yttria-Doped Zirconia in the Nanosecond and Femtosecond Regimes, *J. Appl. Phys.*, 2010, **107**, 014908.

54 J. Noack, R. Tönnies, K. Hohla, R. Birngruber and A. Vogel, Influence of Ablation Plume Dynamics on the Formation of Central Islands in Excimer Laser Photrefractive Keratectomy, *Ophthalmology*, 1997, **104**, 823–830.

55 N. Didden, On the Formation of Vortex Rings: Rolling-up and Production of Circulation, *J. Appl. Math. Phys. (ZAMP)*, 1979, **30**, 101–116.

56 D. Bradley, C. Sheppard, I. Suardjaja and R. Woolley, Fundamentals of High-Energy Spark Ignition with Lasers, *Combust. Flame*, 2004, **138**, 55–77.

57 M. Nishihara, J. B. Freund and G. S. Elliott, A Study of Velocity, Temperature, and Density in the Plasma Generated by Laser-Induced Breakdowns, *J. Phys. D: Appl. Phys.*, 2020, **53**, 105203.

58 S. Shabanov and I. Gornushkin, Modeling Chemical Reactions in Laser-Induced Plasmas, *Appl. Phys. A*, 2015, **121**, 1087–1107.

59 J. Hermann, A. Lorusso, A. Perrone, F. Strafella, C. Dutouquet and B. Torralba, Simulation of Emission Spectra from Nonuniform Reactive Laser-Induced Plasmas, *Phys. Rev. E*, 2015, **92**, 053103.

60 N. Glumac, G. Elliott and M. Boguszko, Temporal and Spatial Evolution of a Laser Spark in Air, *AIAA J*, 2005, **43**, 1984–1994.

61 D. Diaz and D. W. Hahn, Plasma Chemistry Produced during Laser Ablation of Graphite in Air, Argon, Helium and Nitrogen, *Spectrochim. Acta Part B: At. Spectrosc.*, 2020, **166**, 105800.